Atomic-Scale Sources and Mechanism of Nanoscale Electronic Disorder in $Bi_2Sr_2CaCu_2O_{8+\delta}$

K. McElroy,[1,2] Jinho Lee,[1] J. A. Slezak,[1] D.-H. Lee,[2] H. Eisaki,[3] S. Uchida,[4] J. C. Davis[1]*

The randomness of dopant atom distributions in cuprate high–critical temperature superconductors has long been suspected to cause nanoscale electronic disorder. In the superconductor $Bi_2Sr_2CaCu_2O_{8+\delta}$, we identified populations of atomic-scale impurity states whose spatial densities follow closely those of the oxygen dopant atoms. We found that the impurity-state locations are strongly correlated with all manifestations of the nanoscale electronic disorder. This disorder occurs via an unanticipated mechanism exhibiting high-energy spectral weight shifts, with associated strong superconducting coherence peak suppression but very weak scattering of low-energy quasi-particles.

Important new electronic materials have been created by chemically doping their inert parent compounds with charge carriers. Examples include organic conductors, cuprate high-temperature superconductors, manganites that display colossal magnetoresistance, cobaltates that display large thermoelectric powers, and magnetic semiconductors. In such chemical doping schemes, a critical challenge is to generate the desired electronic properties without also creating destructive electronic disorder due to the random distribution of dopant atoms.

Cuprate high-T_c superconductivity (HTSC) is one of the most remarkable examples of this situation. In hole-doped cuprates (those with the highest critical temperature T_c), superconductivity appears when electron acceptor atoms are introduced into the parent insulators (*1*). This process almost always creates random distributions of differently charged dopant atoms near the critical CuO_2 crystal planes. These are potential sources of electronic and crystalline disorder (*2*) and T_c suppression (*3*, *4*). Indeed, dopant atoms may have two diametrically opposite influences on HTSC, being destructive at the atomic scale but supportive globally (via enhanced carrier densities). Thus, a key challenge in cuprate studies has been to determine directly how dopant atoms influence the superconducting electronic structure at the atomic scale.

Spectroscopic imaging scanning tunneling microscopy (SI-STM) studies reveal nanoscale electronic disorder in many cuprates. For example, $YBa_2Cu_3O_{6-\delta}$ exhibits local density of states (LDOS) modulations at the CuO plane (*5*). In $Na_xCa_{2-x}CuO_2Cl_2$, topographic imaging shows both random nanoscale electronic disorder (*6*) and disorder related to the 4×4 electronic "checkerboard" of nondispersive LDOS modulations (*7*). $Bi_2Sr_2CaCu_2O_{8+\delta}$ (Bi-2212) exhibits several signatures of electronic disorder, including subgap dispersive LDOS modulations (*8*), disordered regions (diameter ~3 nm) in energy-gap images $\Delta(\vec{r})$ (*9*–*11*), and nanoscale disorder in low-bias topographic images $z(\vec{r})$ (*11*). Although dopant disorder was suspected to cause these effects, this was impossible to verify directly because simultaneous atomic-resolution images of the dopant atom locations and the superconducting electronic structure were unattainable.

Locating the atomic-scale sources of electronic disorder. Here we focus on Bi-2212, a cuprate superconductor that is hole-doped by adding a number δ of nonstoichiometric oxygen atoms per unit cell. The floating zone–grown crystals, prepared with variable oxygen dopant densities, can be cleaved to reveal the BiO layer (Fig. 1A). Although analyses of x-ray and neutron scattering studies imply that the oxygen dopant atoms may be located either within or between BiO layers (*12*, *13*), their exact locations have never been determined. To attempt location of oxygen dopants by SI-STM, one needs to identify an electronic impurity state characteristic of dopant atoms only. The stoichiometric oxygen atoms are invisible to low-bias SI-STM because their contributions to the BiO band structures occur far from the Fermi energy. By contrast, each nonstoichiometric oxygen dopant atom is a $-2e$ charged impurity, so they might be expected to generate an electronic impurity state somewhat below the Fermi level. To search for such dopant-induced impurity states, we acquired LDOS($\vec{r}$,$E = eV$) images with large field of view over a range of energies -1.2 eV $< E <$ -0.15 eV. At typical tunnel junction resistance $R_J = 10^9$ ohms with $V \sim 1$ V, the electric field exceeds $\sim 10^9$ V/m and can rupture the BiO surface; therefore, new techniques for LDOS imaging with R_J up to 10^{11} ohms were developed for these studies.

Figure 1A shows a typical $z(\vec{r})$ topograph with sample bias $V_B = -0.9$ V. Figure 1B, which shows the simultaneous LDOS($\vec{r}$,E) image at energy $E = -0.9 \pm 0.05$ eV, reveals a random distribution of bright maxima in the LDOS, each with radius ~4 Å. The inset of Fig. 1A compares the shape of the high-voltage spectrum at one of the bright features in Fig. 1B with that of a spectrum typical of regions far from them; we see that the contrast in Fig. 1B occurs because each bright region exhibits a broad peak (arrow in Fig. 1A) in the spectrum at $V = -0.96$ V.

By cross-correlating the simultaneous topographic and LDOS($V = -0.96$ V) images (e.g., Fig. 1A with Fig. 1B), we determined that the "–0.96 eV features" occur at a distance of ~1.9 Å away from the nearest Bi along the BiO bond direction but in an unknown plane (inset, Fig. 1B). The precision of this determination is not high because of crystal spatial disorder and the extended nature (diameter ~8 Å) of the impurity state. One possible explanation for these features is a dopant atom residing above the BiO layer. This scenario, although not ruled out, is not supported by observations of adatoms at these locations. Another possibility is a vacancy at the stoichiometric oxygen site in the BiO layer, but here topography does not reveal the anticipated displacements of Bi atoms. A well-known electronic defect (*4*) is substitution of a Bi atom on the Sr site, but this cannot explain the –0.96 eV impurity state because it is positively charged (Bi^{3+} on the Sr^{2+} site), so its impurity state should exist above the Fermi level; in fact it is observed at $E = +1.7$ eV (*9*). A final possibility is that, at whichever site within the crystal the O^{-2} dopant atom resides, it generates a local electronic impurity state somewhere below the Fermi level.

To test whether the "–0.96 V features" could be such impurity states, we repeated the LDOS($V = -0.96$ V) imaging experiments on several samples with different oxygen dopant densities. Typical results are shown in Fig. 2, where the locations of spectra exhibiting –0.96 V peaks are marked as white dots superimposed on the simultaneously acquired gap maps $\Delta(\vec{r})$. The hole density p per CuO_2 decreases from Fig. 2A to Fig. 2C, as evidenced by the increasing average gap magnitude $\overline{\Delta}$; in break junction studies of Bi-2212, $\overline{\Delta} \approx [75 - 275\ (\pm 10\%) \times p]$ meV (*14*). From images of the –0.96 eV features, we

[1]Laboratory of Atomic and Solid State Physics, Department of Physics, Cornell University, Ithaca, NY 14850, USA. [2]Department of Physics, University of California, Berkeley, CA 94720, USA. [3]National Institute of Advanced Industrial Science and Technology (AIST), 1-1-1 Central 2, Umezono, Tsukuba, Ibaraki 305-8568, Japan. [4]Department of Physics, University of Tokyo, Tokyo 113-8656, Japan.

*To whom correspondence should be addressed. E-mail: jcdavis@ccmr.cornell.edu

find that their density per CuO_2 plaquette, n, also diminishes from Fig. 2A to Fig. 2C and is related to the average gap magnitude $\overline{\Delta} \approx [75 - 600\ (\pm 15\%) \times n]$ meV. These data are all consistent with every –0.96 eV state being associated with the contribution of ~2 holes to the CuO_2 plane. It is then reasonable to postulate that each is due to a single oxygen dopant atom, and hereafter we refer to them provisionally as the "dopant defects." These –0.96 eV impurity states, independent of their microscopic cause or electronic structure, occur at the primary sources of the nanoscale electronic disorder (see below).

Superconducting electronic disorder phenomena in Bi-2212. The simplest type of electronic disorder in Bi-2212 appears in LDOS($\vec{r}$,E) images generated from tip-sample differential tunneling conductance $g(\vec{r},V)$ measurements:

$$\mathrm{LDOS}(\vec{r}, E = eV) \propto g(\vec{r}, V) \equiv dI/dV\big|_{\vec{r},V} \quad (1)$$

Differential conductance images revealed weak quasi-periodic modulations exhibiting up to 16 inequivalent sets of energy-dispersive wave vectors in $g(\vec{q},E)$, the Fourier transform magnitude of $g(\vec{r},E)$ (*8*). When analyzed as scattering-induced quasi-particle interference patterns (*15*–*17*), these sets of dispersing $\vec{q}$-vectors yielded elements of the Fermi surface and momentum space $\Delta(\vec{k})$ in excellent agreement with photoemission (*8*, *18*, *19*). However, the identity of the scattering centers that generate these quasi-particle interference patterns was unknown.

Intense disorder is also universally seen in atomically resolved images of the superconducting energy gap $\Delta(\vec{r})$ (*9*–*11*, *20*–*23*). Gap values range from below 20 meV to above 65 meV within adjacent nanoregions; the data shown in Fig. 2, A to C, are typical. Explaining these $\Delta(\vec{r})$ phenomena has become a key challenge in cuprate studies.

The disorder seen in low-bias (–150 mV < V_B < 0) topographic images of Bi-2212 is also exceptionally strong (*11*). For example, the low-bias topograph in Fig. 3B (with the ~2.6 nm wavelength surface undulations removed by Fourier filtering) reveals the disorder contrast as dark and light nanoregions. STM topographic imaging actually measures the vertical tip displacement $z(\vec{r},V_B)$ required to maintain constant tunnel current $I(V_B)$ for sample bias voltage V_B. With z_0 as the exponential tunneling factor, the current at V_B is given by

$$I(V_B) \propto \exp[-z(\vec{r}, V_B)/z_0] \times \int_0^{eV_B} \mathrm{LDOS}(E, \vec{r})\,dE \quad (2)$$

$$\Rightarrow z(\vec{r}, V_B) + C = z_0 \ln \int_0^{eV_B} \mathrm{LDOS}(E, \vec{r})\,dE \quad (3)$$

In this simple single-particle picture, the spatial charge density variations within states up to $E = eV_B$ would then be

$$\delta\rho(\vec{r})\Big|_0^{eV_B} = \delta\left[e\int_0^{eV_B} \mathrm{LDOS}(E, \vec{r})\,dE\right] \quad (4)$$

For this reason, the disorder seen in low-bias topographs $z(\vec{r}, -150\ \mathrm{mV} < V_B < 0)$ has been interpreted via Eqs. 3 and 4 as a logarithmic image of charge density disorder (*11*, *24*).

Modeling the cause of nanoscale electronic disorder in cuprates. Nanoscale electronic disorder effects in cuprates (*5*–*11*, *20*–*23*) pose critically important questions. Are there really intense nanoscale CuO_2 plane charge density variations in near-optimal high-T_c superconductors? Is the observed electronic disorder due to some form of electronic self-organization or to dopant disorder? If the latter, what is the microscopic mechanism? Is it scattering from dopant atoms that produces the quasi-particle interference modulations (*8*) and superconducting coherence peak suppression (*10*, *22*, *23*)? Which specific dopant atom or defect locations most strongly diminish T_c (*3*, *4*)?

Theoretical studies of the effects of dopant atoms explore several hypotheses. In one such model (*24*–*26*), poor electrostatic screening of the –2e charge on each dopant atom produces a repulsive potential for electrons, causing holes to accumulate at that location. This local increase in hole density produces reduced energy-gap values near the dopant atoms (*24*–*26*). Thus, in such a "hole accumulation" model, the disorder in $\Delta(\vec{r})$ is created electrostatically by the dopant atoms via hole density variations in the CuO_2 plane. The second class of model (*27*) holds that, because of their displacement from the CuO_2 plane, the dopant oxygens produce only small-angle scattering, which is nonetheless sufficient to result in both the observed quasi-particle interference modulations and the gap disorder (*27*). A third model is that the dopants generate local crystalline stress/strain at the nanoscale (*2*, *3*, *28*, *29*). In

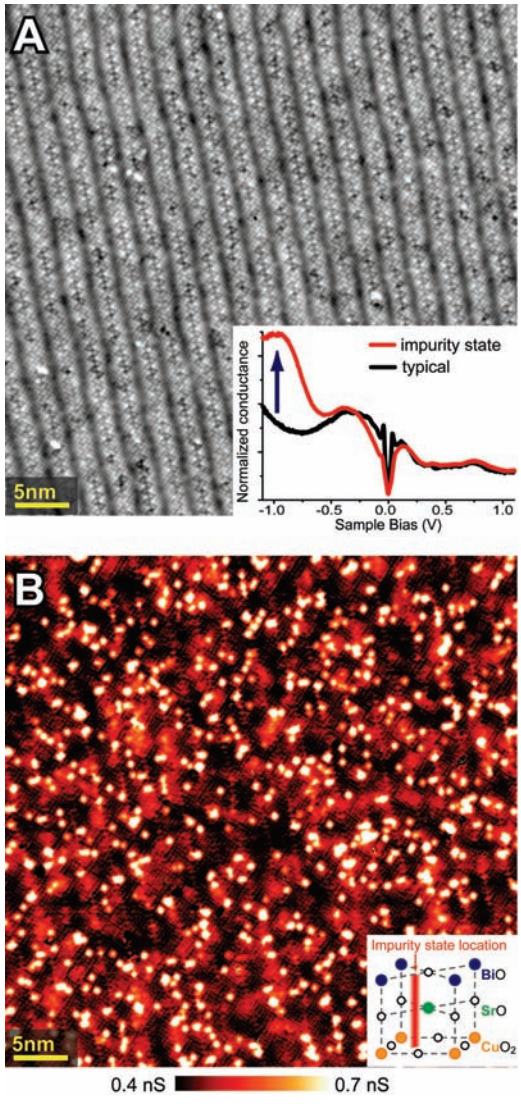

Fig. 1. (**A**) Atomic-resolution topographic image of the BiO surface of Bi-2212 taken at V_B = –0.9 V and $R_J = 3 \times 10^{10}$ ohms. The inset compares the shape of a high-voltage spectrum at one of the bright features in (B) with that of a spectrum typical of regions far from any bright feature (spectra were taken at different junction resistance and have different normalizations). (**B**) An LDOS(E = –0.96 eV,$\vec{r}$) ≡ O($\vec{r}$) image [simultaneously acquired with (A)] of the differential tunneling conductance measured at V = –0.9 V with a modulation amplitude of 50 mV. It shows about 600 atomic-scale regions of high differential conductance, which occur because there is a peak in the differential conductance spectrum near V = –0.96 V at each of these locations. This is the only energy in our window where such effects were detected. Examples of the high-voltage spectra on and off these bright regions are shown in the inset of (A); an arrow indicates the peak in tunnel conductance. Shown schematically in the inset of (B) is the line parallel to the c axis along which we believe the dopant defect is located. It is not possible to determine which layer of the crystal it lies in.

this picture, the local electronic disorder occurs because various hopping matrix elements in the crystalline unit cell are altered by crystal distortions near dopants. It seemed reasonable that the exact cause of cuprate nanoscale electronic disorder could contain some contributions from all these, and perhaps other, effects.

Correlating dopant defect locations with electronic disorder. To explore these issues, we acquired simultaneous atomically resolved (i) topographs $z(\vec{r},V_B)$, (ii) LDOS$(E,\vec{r})$ images, (iii) gap maps $\Delta(\vec{r})$, and (iv) LDOS$(E = -0.96$ eV$,\vec{r}) \equiv O(\vec{r})$ dopant-defect images for each sample (more than 3×10^5 individual spectra for this study). To analyze such data, we define the normalized cross-correlation $C_{f,g}(\vec{R})$ between two-dimensional images $f(\vec{r})$ and $g(\vec{r})$ as

$$C_{f,g}(\vec{R}) = \frac{\int \left[f(\vec{r}) - \bar{f}\right] \times \left[g(\vec{r}+\vec{R}) - \bar{g}\right] d^2r}{\sqrt{A_{f,f}(0)A_{g,g}(0)}} \quad (5)$$

where

$$A_{f,f}(\vec{R}) = \int \left[f(\vec{r}) - \bar{f}\right] \times \left[f(\vec{r}+\vec{R}) - \bar{f}\right] d^2r \quad (6)$$

For simplicity, we designate $C_{f,g}(\vec{R} = 0)$ as $C[f{:}g]$. Identical images $f(\vec{r}) = g(\vec{r})$ yield $C[f{:}g] = 1$, an image and its negative $f(\vec{r}) = -g(\vec{r})$ yield $C[f{:}g] = -1$, and $C[f{:}g] = 0$ for no local correlation. We calculate a series of cross-correlations between the simultaneously measured $z(\vec{r},V_B)$, LDOS$(E,\vec{r})$, $\Delta(\vec{r})$, and $O(\vec{r})$ images, yielding similar results at all dopings studied. A typical set of $C_{f,g}(\vec{R})$ data averaged azimuthally (Fig. 3A) immediately reveals the strong spatial correlations between dopant defects and the electronic disorder.

Important deductions emerge from more detailed analysis of these cross-correlations. It is well known that low-bias topographic disorder and gap maps are anticorrelated (*11*), and Fig. 3A shows that our measured cross-correlation coefficient between $\Delta(\vec{r})$ and $z(\vec{r},V_B = -100$ mV), $C[\Delta(\vec{r}){:}z(\vec{r},V_B = -100$ mV)] ≈ -0.4, in good agreement. But we can now demonstrate that this effect is indeed generated by dopant defects, because (Fig. 2, A to C; Fig. 3A) strong correlations exist between dopant defect images $O(\vec{r})$ and both (i) low-bias topographic disorder $z(\vec{r},V_B = -100$ mV), $C[O(\vec{r}){:}z(\vec{r},V_B = -100$ mV)] ≈ -0.25, and (ii) simultaneous gap maps $\Delta(\vec{r})$, $C[O(\vec{r}){:}\Delta(\vec{r})] \approx +0.3$. But these correlations are inconsistent with dopant-induced hole accumulation models (*24*–*26*) because the sign of the correlation $C[O(\vec{r}){:}\Delta(\vec{r})]$ is positive. This means that instead of diminished gap magnitudes, we find predominantly increased gap magnitudes near each dopant defect (Fig. 2, A to C; Fig. 3A). We find that the sign of $C[O(\vec{r}){:}z(\vec{r},V_B)]$ is negative for both signs of sample bias. This means that low-bias $z(\vec{r},V_B)$ is almost equally diminished for states above and below the Fermi energy. Even more important, as V_B is increased, correlations with pairs of topographs of opposite V_B remain identical, but the topographic $z(\vec{r},V_B)$ disorder itself begins to moderate near $V_B = \pm 0.25$ V and is greatly diminished above $V_B = \pm 0.60$ V (Fig. 3C). Consistent with this, Fig. 3A shows that $C[O(\vec{r}){:}z(\vec{r},V_B = -900$ mV)] ≈ 0 because disorder in $z(\vec{r},V_B = \pm 0.9$ V) is very weak. All these data indicate that, when integrated over states in the range $V_B \approx \pm 0.9$ V, variations in $\int_0^{eV_B}$ LDOS$(E,\vec{r})dE$ are significantly weaker than had been originally suspected [as had been anticipated from nuclear magnetic resonance studies (*30*, *31*)]. Within the single-particle picture, we estimate that root mean square charge density fluctuations are $\delta\rho(\vec{r})/\rho \leq 10\%$ in the states up to $V_B \approx \pm 0.9$ V.

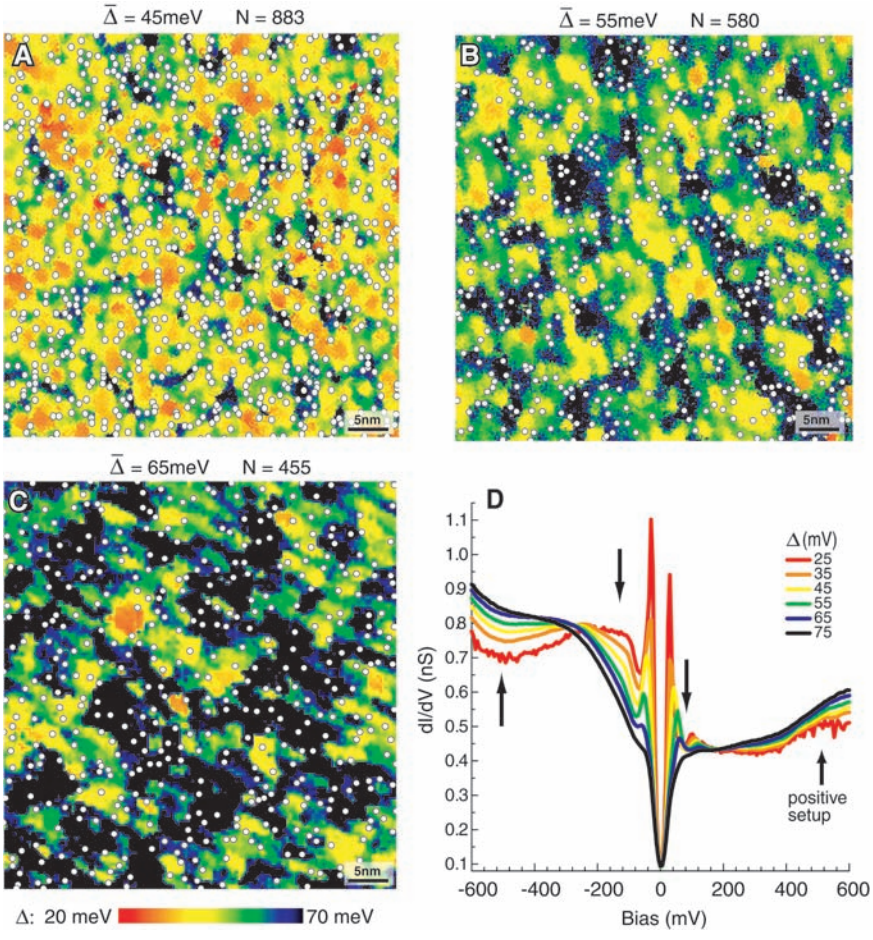

Fig. 2. (**A** to **C**) Three gap maps, with identical field of view sizes of 49 nm (corresponding to ~16,000 CuO_2 plaquettes) and color scales, measured on samples with three different oxygen doping levels. Average gap magnitudes $\bar{\Delta}$ are shown at the top, together with values of *N*, the total number of –0.96 V features (shown as white circles) in the field of view. Those in (**B**) were derived from the LDOS image in Fig. 1B. Note that the black regions have a distinct spectrum with a wide gap and no superconducting coherence peaks (*23*), as also shown by the black curve in (**D**). (**D**) The average spectrum associated with each superconducting gap value is color-coded to associate each gap-average spectrum with regions of the same color in all gap maps. As coherence peaks decrease and local gap values increase near dopant defects, the spectral weight shifts from below to above 250 meV for filled states and from below to above 150 meV for empty states. To make these observations, we used setup voltages of +600 meV and –600 meV, yielding simultaneous topographs with minimal nanoscale disorder and almost identical sets of spectra. Thus, no renormalization of these spectra to compensate for topographic disorder (*11*) was required. Further, the –600 meV setup voltage is sufficiently far below the –960 meV peak at the dopant sites to avoid tip elevation errors due to the impurity states.

How do the dopant defects generate the electronic disorder? Because disorder in topography clearly exists at low-bias $V_B \leq \pm 0.25$ V but diminishes markedly above $V_B \approx \pm 0.60$ V, the low-bias electronic disorder must be compensated by contributions of the opposite sign beginning above $V_B \approx \pm 0.25$ V. This can occur only if the low-energy LDOS spectral weight diminutions near dopant defects are balanced by equal enhancements at intermediate energies. To test this deduction, we measured LDOS$(\vec{r},E)$ images up to high voltage (but well below the ~ –0.96 eV impurity state) and

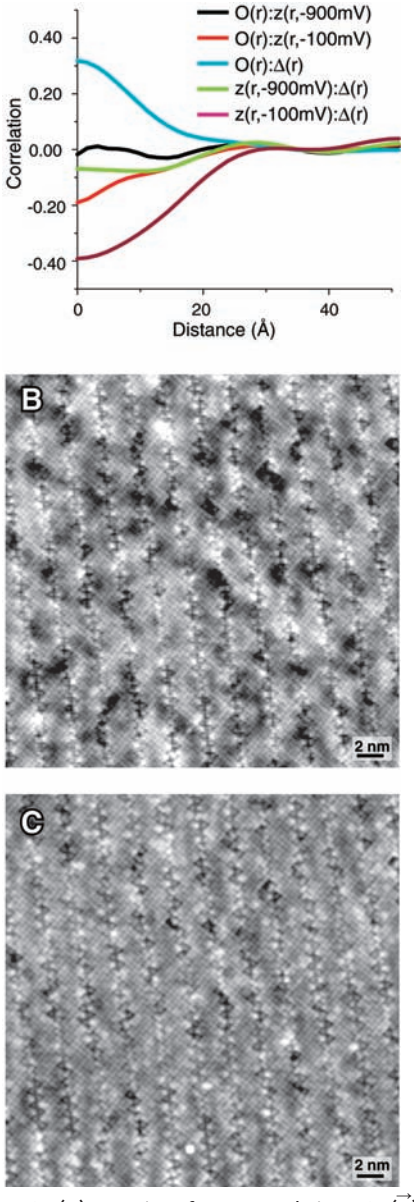

Fig. 3. (**A**) A series of cross-correlations $C_{f,g}(\vec{R})$ among the simultaneously measured $z(\vec{r},V_B)$, $\Delta(\vec{r})$, and $O(\vec{r})$ images. These show the angular average $C_{f,g}(|\vec{R}|)$ for *f*:*g* pairs $O(\vec{r})$:$\Delta(\vec{r})$ (blue line), $O(\vec{r})$:$z(\vec{r},V_B = -100$ meV) (red line), $O(\vec{r})$:$z(\vec{r},V_B = -900$ meV) (black line), $\Delta(\vec{r})$:$z(\vec{r},V_B = -100$ meV) (purple line), and $\Delta(\vec{r})$:$z(\vec{r},V_B = -900$ meV) (green line). We note that because $O(\vec{r})$ is an image with intensity in only a few percent of this field of view (see Fig. 1B), any correlation $C[O(\vec{r}), f(\vec{r})] \sim 0.3$ is actually quite strong. The images in Fig. 2, A to C, show directly that the $O(\vec{r})$:$\Delta(\vec{r})$ correlation, while strong, is not obviously deterministic, as might be expected for a nonlocal quantum mechanical system. (**B**) A typical low-bias topographic image $z(\vec{r},V_B = -100$ mV), with the 2.6 nm "supermodulation" surface undulation removed but retaining the crystalline structure, and showing the low-bias disorder as dark patches. (**C**) A high-bias topographic image $z(\vec{r},V_B = -900$ mV), from the same field of view as (B) with the same gray scale, with the 2.6 nm "supermodulation" surface undulation removed but retaining the crystalline structure. Here, minimal nanoscale electronic disorder can be detected.

identified the average spectrum associated with each superconducting gap value. The results (Fig. 2D) are color-coded to associate each gap-averaged spectrum with regions of the same color in all gap maps. These shifts are correlated with dopant defect locations to the same degree that the gap map is (Fig. 2, A to C; Fig. 3A, blue line). Therefore, as coherence peaks are suppressed and local gap values increase near dopant defects (Fig. 2, A to C; Fig. 3A), spectral weight shifts from below to above $E = 250$ meV for filled states and $E = 150$ meV for empty states are seen (arrows, Fig. 2D). Total spectral weight is conserved within the range $|E| < 0.9$ eV. These effects are most easily detected at intermediate doping ($p \approx 0.14$); we anticipate that they will diminish at very low and very high doping.

Because charge density variations are significantly weaker than previously suspected, a non–charge-driven mechanism for the nanoscale electronic disorder effects should be considered. It is known that substitutional atomic disorder at the Sr site suppresses superconductivity strongly (*4*), most likely by distortions of the crystalline unit cell and associated changes in the hopping matrix elements and superconducting correlations (*2*–*4*, *28*, *29*). Dopant atoms might act similarly, perhaps by displacing the Sr or apical oxygen atoms nearby, thereby changing the vibration frequencies and/or hopping integrals. Very recently, on the basis of the results reported here, Nunner *et al*. proposed a new model for the cuprate electronic disorder mechanism (*32*) in which the dopants not only produce some charge disorder, but also strongly perturb the local superconducting pairing potential on individual bonds between Cu sites. This proposal, that atomic-scale electron pairing–potential variations are paramount, offers a novel explanation for the complex phenomenology described here and in (*8*–*11*, *20*–*23*).

Correlating dopant defects with quasiparticle interference modulations. Another long-standing mystery has been the source of the very weak low-energy quasi-particle scattering interference modulations (*8*) and

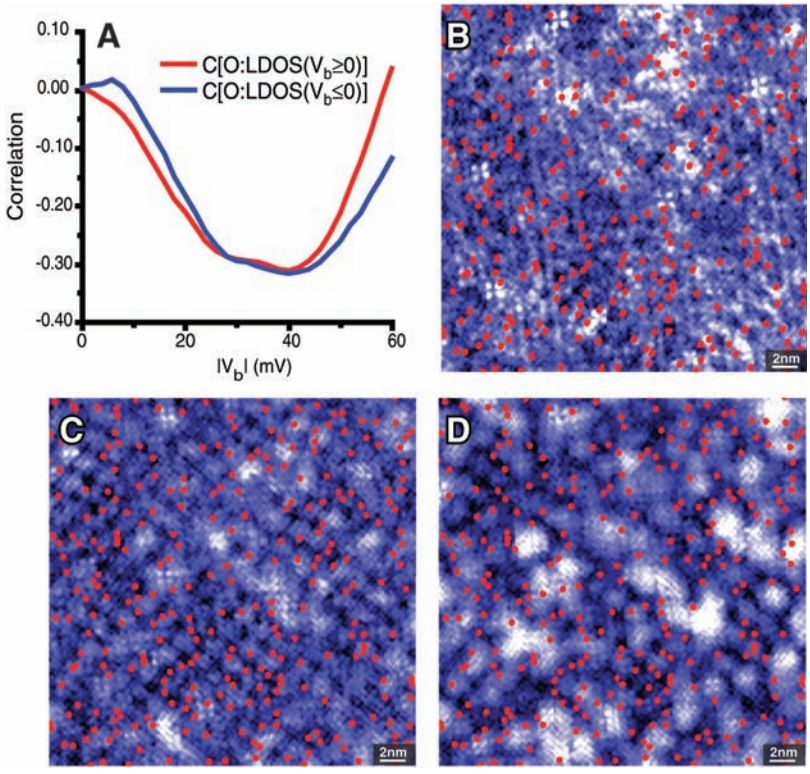

Fig. 4. (**A**) $R = 0$ cross-correlation values $C[O(r),LDOS(r,E)]$ for all energies $|E| < 60$ meV. These correlations begin to be significant around $E = 10$ meV and are intense for 30 meV $< |E| <$ 50 meV. The sign is always negative; hence, LDOS is low when the intensity of the –0.96 V peak in the $O(\vec{r})$ map (e.g., Fig. 1B) is high. This is true even though the LDOS modulation images look completely different at energies that differ by less than 10 meV. (**B**) Image of oxygen dopant defect locations (red dots) and LDOS at $E = -14$ meV. The modulations are weak at this energy and consist of numerous wave vectors. Nonetheless, the tendency for the dopant defects to lie in the minima of LDOS modulations can be detected by eye. (**C**) Image [simultaneous with (B) and (D)] of dopant defect locations and LDOS at $E = -24$ meV. Here the modulations are strong and more clearly reveal the tendency for the dopants to be at the minima. (**D**) Image [simultaneous with (B) and (C)] of dopant defect locations and LDOS at $E = -34$ meV. Here the long-wavelength modulations no longer exist, and the contrast basically represents the height of the –34 meV coherence peaks. The tendency for these peaks to be strongly diminished where the dopants are clustered is obvious.

the much stronger superconducting coherence peak suppressions (*8*, *10*, *22*, *23*) in Bi-2212. The analysis of correlations between the dopant defects and quasi-particle interference patterns $C[O(\vec{r}):LDOS(\vec{r},E)]$ shown in Fig. 4A reveals directly that they are strongly correlated over a wide energy range. The negative sign of these correlations means that minima of LDOS modulations preferentially occur at the dopant defects. This is true at all energies, even though the actual quasi-particle interference patterns are quite different (*8*). This can be seen directly in images of $LDOS(\vec{r},E)$ at $E = -14$ meV, -24 meV, and -34 meV (Fig. 4, B to D, respectively), with dopant defect locations shown as red dots. In all cases we see that the dopant defects have a very high probability of being found at the minima in the LDOS, even though the patterns are quite different between energies. This implies a fixing of the spatial phase of the LDOS modulations at scattering sites, an effect first seen in cuprates at oxygen vacancy defects in $YBa_2Cu_3O_{6-\delta}$ (*5*). Perhaps more important, Fig. 4D shows that suppression of superconducting coherence peaks is found primarily near the dopant defect clusters, and the bright regions with the sharp coherence peaks—usually associated with strong superconductivity—occur between them. The correspondence between dopant defect locations and LDOS minima for a variety of LDOS patterns occurring at different energies (Fig. 4) provides clear and direct evidence that these dopant defects generate the LDOS modulations and also suppress superconducting coherence peaks in Bi-2212.

Our simultaneous imaging of apparent dopant-induced impurity states and superconducting electronic structure points to solutions for several outstanding problems. The results provide direct evidence for the concept of an atomic-scale source for the nanoscale electronic disorder in cuprates (*11*, *24–26*). Strong correlations between dopant defect distributions and both gap map and coherence peak amplitude show that the dopant defects are responsible for most (but perhaps not all) of the superconducting electronic disorder in Bi-2212. Further, scattering leading to quasi-particle interference can now be ascribed almost completely to whichever atomic-scale perturbation produces the dopant defects. Finally, the topographic disorder and related superconducting electronic disorder are due empirically to spectral weight shifts from low to high energy near each dopant defect. These data indicate that high-energy spectral weight redistributions, strong coherence peak suppressions, and very weak scattering of low-energy quasi-particles are dominant elements in the atomic-scale mechanism of superconducting electronic disorder in $Bi_2Sr_2CaCu_2O_{8+\delta}$. Similar phenomena are likely to be common in all nonstoichiometric oxygen-doped high-T_c cuprates.

References and Notes

1. S. Maekawa *et al.*, *Physics of Transition Metal Oxides* (Springer-Verlag, Berlin, 2004).
2. R. J. Cava, *Nature* **394**, 126 (1998).
3. J. P. Attfield, A. L. Kharlanov, J. A. McAllister, *Nature* **394**, 157 (1998).
4. H. Eisaki *et al.*, *Phys. Rev. B* **69**, 064512 (2004).
5. H. L. Edwards *et al.*, *Phys. Rev. Lett.* **75**, 1387 (1995).
6. Y. Kohsaka *et al.*, *Phys. Rev. Lett.* **93**, 097004 (2004).
7. T. Hanaguri *et al.*, *Nature* **430**, 1001 (2004).
8. K. McElroy *et al.*, *Nature* **422**, 520 (2003).
9. G. Kinoda *et al.*, *Phys. Rev. B* **67**, 224509 (2003).
10. K. M. Lang *et al.*, *Nature* **415**, 412 (2002).
11. S. H. Pan *et al.*, *Nature* **413**, 282 (2001).
12. D. Grebille *et al.*, *Acta Crystallogr.* **B52**, 628 (1996).
13. W. Que, M. B. Walker, *Phys. Rev. B* **46**, 14772 (1992).
14. N. Miyakawa *et al.*, *Phys. Rev. Lett.* **80**, 157 (1998).
15. Q.-H. Wang, D.-H. Lee, *Phys. Rev. B* **67**, 020511 (2003).
16. L. Capriotti, D. J. Scalapino, R. D. Sedgewick, *Phys. Rev. B* **68**, 014508 (2003).
17. L. Zhu, W. A. Atkinson, P. J. Hirschfeld, *Phys. Rev. B* **69**, 060503 (2004).
18. U. Chatterjee *et al.*, available at http://arXiv.org/abs/cond-mat/0505296.
19. K. McElroy *et al.*, available at http://arXiv.org/abs/cond-mat/0505333.
20. T. Cren *et al.*, *Europhys. Lett.* **54**, 84 (2001).
21. A. Matsuda *et al.*, *Physica C* **388**, 207 (2003).
22. C. Howald, P. Fournier, A. Kapitulnik, *Phys. Rev. B* **64**, 100504 (2001).
23. K. McElroy *et al.*, *Phys. Rev. Lett.* **94**, 197005 (2005).
24. Z. Wang *et al.*, *Phys. Rev. B* **65**, 064509 (2002).
25. Q.-H. Wang, J. H. Han, D.-H. Lee, *Phys. Rev. B* **65**, 054501 (2002).
26. I. Martin, A. V. Balatsky, *Physica C* **357–360**, 46 (2001).
27. D. J. Scalapino, T. S. Nunner, P. J. Hirschfeld, in *Proceedings of the 7th International Conference on Spectroscopies in Novel Superconductors* (*Sitges, Spain*), in press (available at http://arXiv.org/abs/cond-mat/0409204).
28. J.-X. Zhu *et al.*, *Phys. Rev. Lett.* **91**, 057004 (2003).
29. E. Kaneshita, I. Martin, A. R. Bishop, *Phys. Soc. Jpn. Lett.* **73**, 3223 (2004).
30. J. Bobroff *et al.*, *Phys. Rev. Lett.* **89**, 157002 (2002).
31. J. W. Loram, J. L. Tallon, W. Y. Liang, *Phys. Rev. B* **69**, 060502 (2004).
32. T. Nunner *et al.*, available at http://arXiv.org/abs/cond-mat/0504693.

33. We thank W. Atkinson, A. V. Balatsky, A. Bishop, J. C. Campuzano, R. J. Cava, P. Hirschfeld, J. E. Hoffman, V. Madhavan, R. Markiewicz, T. M. Rice, G. Sawatzky, D. J. Scalapino, Z.-X. Shen, Z. Wang, and A. Yazdani for helpful conversations and communications. Supported by the Office of Naval Research, NSF, and Cornell University.

4 April 2005; accepted 30 June 2005
10.1126/science.1113095

FD, a bZIP Protein Mediating Signals from the Floral Pathway Integrator FT at the Shoot Apex

Mitsutomo Abe,[1]* Yasushi Kobayashi,[1,2]*† Sumiko Yamamoto,[1,2]* Yasufumi Daimon,[1] Ayako Yamaguchi,[1] Yoko Ikeda,[1] Harutaka Ichinoki,[1] Michitaka Notaguchi,[1] Koji Goto,[2,3] Takashi Araki[1,2,4]‡

***FLOWERING LOCUS T* (*FT*) is a conserved promoter of flowering that acts downstream of various regulatory pathways, including one that mediates photoperiodic induction through *CONSTANS* (*CO*), and is expressed in the vasculature of cotyledons and leaves. A bZIP transcription factor, FD, preferentially expressed in the shoot apex is required for FT to promote flowering. FD and FT are interdependent partners through protein interaction and act at the shoot apex to promote floral transition and to initiate floral development through transcriptional activation of a floral meristem identity gene, *APETALA1* (*AP1*). *FT* may represent a long-distance signal in flowering.**

Flowering in *Arabidopsis* is regulated by several pathways that converge on the transcriptional regulation of the floral pathway integrators *FT*, *SUPPRESSOR OF OVEREXPRESSION OF CO 1* (*SOC1*), and *LEAFY* (*LFY*) (*1*). *FT* is a direct target of CO, a key transcriptional regulator of the photoperiod pathway, and the role of *FT* as a potent promoter of flowering in response to photoperiods is conserved in *Arabidopsis* and rice (*2–6*). *FT* is expressed in the phloem tissues of cotyledons and leaves (*7*, *8*) and encodes a 20-kD protein with homology to phosphatidylethanolamine binding protein or Raf kinase inhibitor protein (*2*, *3*). However, the biochemical function of FT and downstream events leading to floral transition and floral morphogenesis at the shoot apex remain unknown.

bZIP protein FD is required for FT function. To understand how signals are mediated from *FT* to finally cause floral transition and floral morphogenesis, we searched for genes required for *FT* to promote flowering. Ectopic

[1]Department of Botany, Graduate School of Science, Kyoto University, Sakyo-ku, Kyoto 606-8502, Japan. [2]CREST, Japan Science and Technology Agency, Kawaguchi 332-0012, Japan. [3]Research Institute for Biological Sciences Okayama, Okayama 716-1241, Japan. [4]Adjunct Division of Applied Genetics, National Institute of Genetics, Mishima 411-8540, Japan.

*These authors contributed equally to this work.
†Present address: Department of Molecular Biology, Max Planck Institute for Developmental Biology, D-72076 Tübingen, Germany.
‡To whom correspondence should be addressed. E-mail: taraqui@cosmos.bot.kyoto-u.ac.jp